npj | computational materials

Article

Published in partnership with the Shanghai Institute of Ceramics of the Chinese Academy of Sciences

https://doi.org/10.1038/s41524-025-01663-w

High-density natural active sites for efficient nitrogen reduction on Kagome surfaces promoted by flat bands

Check for updates

Yuyuan Huang[1,2], Yanru Chen[1,2], Shunhong Zhang[1,2], Zhenyu Zhang[1,2] ✉ & Ping Cui[1,2] ✉

Recent studies have shown that single- or few-atom catalysts, with local states near the Fermi level, can promote nitrogen activation and the entire electrocatalytic nitrogen reduction reaction (eNRR) process, but are facing limitations in loading densities and stability. Here, we conceptualize that the Kagome metals featuring naturally abundant surface sites and flat bands are promising candidates to catalyze eNRR. Using first-principles calculations, we first show that the Kagome termination of the prototypical FeSn is accompanied by the presence of flat bands from the Fe-d_{z^2} and d_{xz}/d_{yz} orbitals, and the exposed surface can strongly chemisorb N_2 with an adsorption energy of ~−0.7 eV. The limiting potential of 0.31 V indicates superior eNRR catalytic activity. The mutual independence between neighboring reactive sites also ensures an exceptionally high 25% atomic utilization within the Kagome layer, with each active site possessing high selectivity of eNRR. Our detailed analysis further reveals the critical role of the flat bands in boosting catalytic activity, which is also generalized to the isostructural CoSn and FeGe Kagome systems. Collectively, this work not only enhances the functionalities of Kagome materials for applications but also integrates flat band physics with single-atom catalysis, offering new opportunities in catalyst design.

Electrocatalytic nitrogen reduction reaction (eNRR) has garnered significant attention as a crucial process for ammonia production and related applications[1–3]. In contrast to the main industrial Haber-Bosch process for producing ammonia under high temperature and pressure, the eNRR operates efficiently under milder conditions and consumes less carbon[2–4]. In this catalytic process, chemical changes take place through successive hydrogenation reactions to break the N≡N triple bond, including the distal and alternating pathways[3]. In the eNRR process, it is crucial that the catalyst must be able to chemically activate N_2, an inert gas that does not adsorb on the surfaces of most materials[5–7]. It is therefore highly significant to search for efficient eNRR catalysts and explore related catalytic mechanisms.

In pursuit of potential catalysts, two noble metals, Ru and Re, have been identified as promising catalysts for eNRR among the transition metals[8,9]. However, these systems not only exhibit higher limiting potentials along the reaction trajectories but also show poor selectivity compared to the competing hydrogen evolution reaction (HER) process. Single-atom catalysts (SACs) exhibit advantage due to their cost-effectiveness and versatile tunability, and have attracted significant attention since the conceptual inception[10–12]. In the context of eNRR, localized electronic states of the SACs near the Fermi level facilitate N_2 adsorption and promote completion of the reaction process. For example, it was proposed that FeN_3-embedded graphene can be a catalyst for eNRR based on first-principles calculations[13]. Subsequently, g-C_3N_4 and defective boron nitride monolayers have also been predicted as eNRR catalysts within the context of SACs[14–16]. In addition, catalytic mechanisms involving diatomic or triatomic configurations have further been proposed for eNRR[17–23]. Despite the advantages of discrete atoms for precise control of the active sites, it is still demanding to discover new types of catalysts with high-density (or high-loading) and highly efficient active sites. However, achieving high loadings of SACs represents a new challenge, because such SACs in close proximity can lead to interatomic couplings and cluster formation[24]. Furthermore, ensuring catalytic stability of the anchored SACs presents another challenging aspect[25,26].

Based on these earlier developments, we infer that materials featuring both naturally dispersed atoms and localized electronic states may serve as promising candidates for catalyzing eNRR. These considerations direct us to

[1]International Center for Quantum Design of Functional Materials (ICQD), Hefei National Research Center for Physical Sciences at the Microscale, University of Science and Technology of China, Hefei, Anhui, 230026, China. [2]Hefei National Laboratory, University of Science and Technology of China, Hefei, Anhui, 230088, China. ✉e-mail: zhangzy@ustc.edu.cn; cuipg@ustc.edu.cn

the actively investigated Kagome materials. In this new class of quantum materials, their two-dimensional (2D) Kagome lattices possess a triangular structure of the transition metal atoms. Furthermore, these lattices exhibit geometric frustrations, which lead to a rich spectrum of unconventional electronic properties, including nontrivial topology, van Hove singularities, and, most notably, flat electronic bands[27–31]. Specifically, $Co_3Sn_2S_2$ exhibits giant anomalous Hall effect and Weyl topology[32,33], and Fe_3Sn_2 hosts Dirac fermions[34]. In particular, the FeSn[35–39], CoSn[40–42], and FeGe systems feature flat electronic bands and nontrivial band topology[43–45]. Beyond such physical properties, the catalytic activity of $Co_3Sn_2S_2$ in oxygen evolution reaction (OER) has also been investigated[46], emphasizing the pivotal role of the topological surface states in enhancing the catalytic performance[47,48].

In the present study, our primary emphasis is to investigate the potential role of the flat band characteristics of Kagome materials in facilitating the eNRR by integrating the flat band physics with SACs. Through such a conceptual integration, we aim to identify efficient eNRR catalysts within the Kagome materials, while fundamentally overcoming the severe limitations encountered by the artificially anchored single- or few-atom catalysts. Specifically, we employ first-principles calculations to demonstrate that the appropriately terminated surface of the Kagome metal FeSn can serve as a highly efficient catalytic platform for eNRR, featuring naturally abundant active sites, high catalytic stability and high chemical selectivity. We first identify the naturally occurring 2D Kagome surface through cleavage, and such a termination is accompanied by surface flat electronic bands stemming from the Fe-d_{z^2} and d_{xz}/d_{yz} orbitals. We further demonstrate that N_2 can strongly chemisorb atop an Fe atom in the Kagome surface layer. Moreover, the limiting potential along the entire reaction pathway is calculated to be only 0.31 V within the distal mechanism, highlighting the superior eNRR catalytic performance[3]. Our analysis of the electronic structure variations and magnetic properties underscores the pivotal role of the flat bands in the catalytic activity. The mutual independence between neighboring reactive sites also ensures an exceptionally high 25% atomic utilization within the Kagome layer. In addition, the high selectivity of eNRR over potential competing HER is validated through our detailed studies. We also generalize our design principle for efficient eNRR catalysts to the isostructural CoSn and FeGe Kagome systems, which further demonstrate the crucial role of the flat electronic bands. Collectively, this work not only effectively enhances the functionalities of Kagome materials for important practical applications but also integrates flat band physics with single-atom catalysis, offering new opportunities in catalyst design.

Results

Atomic and electronic structures of Kagome-terminated FeSn

We start by investigating the feasibility of exposing the Kagome termination in FeSn. As shown in Fig. 1a, b, FeSn consists of alternating layers of Fe_3Sn and Sn_2, with the Fe atoms in the Fe_3Sn layer forming a Kagome structure. The interlayer interaction is limited to Fe_3Sn–Sn_2, thus, cutting FeSn along the (001) direction will result in the coexistence of both Sn_2 and Fe_3Sn surface terminations, as confirmed experimentally[35–39]. Furthermore, a Kagome layer is separated from the Sn layer by approximately an interlayer distance of 2.2 Å, suggesting relatively weak interlayer coupling. Thus, FeSn provides a favorable platform for investigating the catalytic properties on a quasi-two-dimensional Kagome lattice. Similar findings are also applicable to the isostructural Kagome systems of FeGe and CoSn[42,44]. In contrast, several other widely studied Kagome systems, such as $Co_3Sn_2S_2$ and AV_3Sb_5, cannot be readily prepared to expose their Kagome terminations[32,49].

Next, we turn our attention to the electronic structure of the Kagome-terminated FeSn. In Fig. 1c, d, we present the orbital-resolved band structure and projected density of states (PDOS) for FeSn with the Fe_3Sn Kagome termination, respectively. Within the energy range of −0.3 to −0.1 eV, discernible flat bands are observed, primarily originating from the contributions of the Fe-d_{z^2} and d_{xz}/d_{yz} orbitals. Such flat bands derived from the localized electronic states have been experimentally confirmed[35,37,38]. We also note that the flat bands exhibit spin-polarized features, which are expected to play a crucial role in breaking the triple bond of the nitrogen molecule[13,18,50].

Adsorption of N_2 on Kagome-terminated FeSn

Based on density functional theory (DFT) calculations (with calculation details given in Part I of the Supplementary Information (SI)), we investigate the adsorption of a N_2 molecule on the Kagome termination of FeSn. First, we examine four distinct adsorption sites: (1) on-top sites of the surface Fe atoms, (2) bridge sites of the Fe atoms, (3) hollow sites of the Fe atoms, and (4) on-top sites of the surface Sn atoms, as shown in Supplementary Fig. S1. Our calculations indicate that N_2 can strongly chemisorb on the on-top site of a surface Fe atom, with an adsorption energy of −0.74 eV, while showing instability at the other three sites. In Fig. 2a, we present the adsorption configuration along with the distribution of charge density differences. We see that N_2 can adsorb on the adsorption site in an end-on configuration, bonded to Fe, representing a widely studied back-donation adsorption

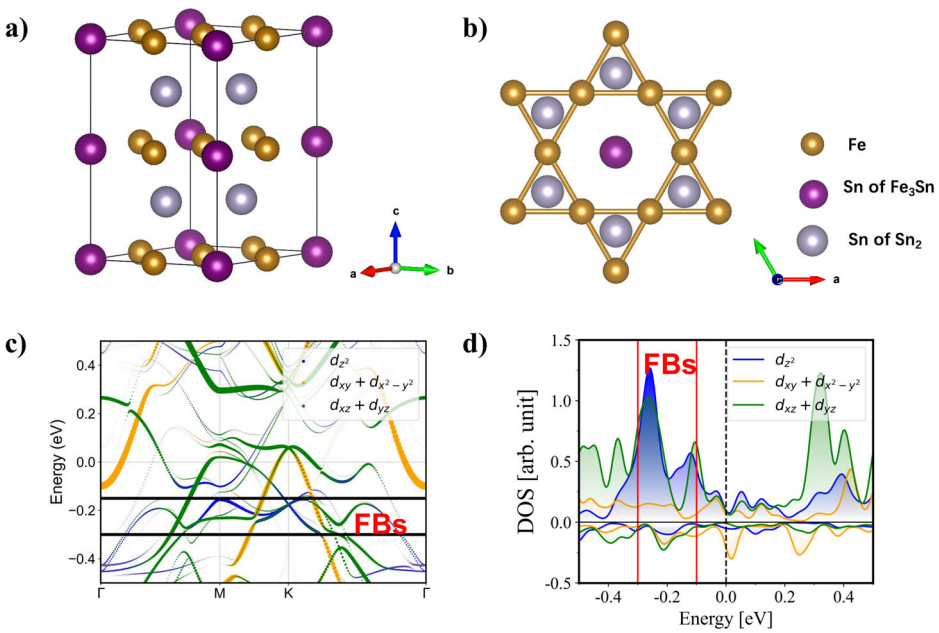

Fig. 1 | Atomic and electronic structures of Kagome-terminated FeSn. a Crystal structure of FeSn. **b** Top view of the Kagome surface. **c** Orbital-resolved band structure and **d** projected density of states (PDOS) for the Kagome termination of FeSn. The highlighted regions by two black lines in (**c**) and two red lines in (**d**) mark the flat bands (FBs).

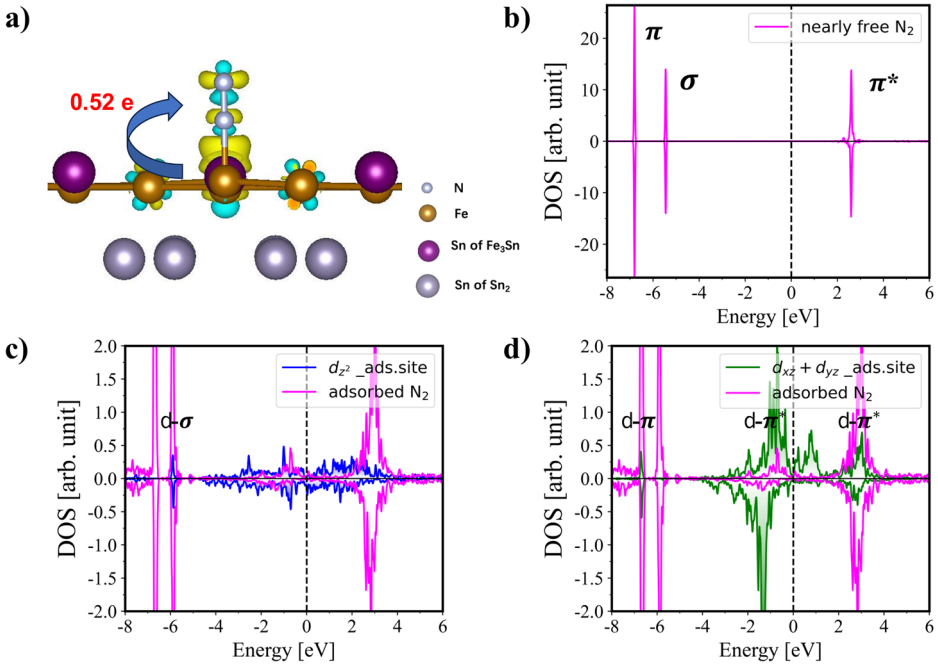

Fig. 2 | Atomic structure and electronic property analysis of N_2 adsorption on Kagome-terminated FeSn. a Adsorption configurations of N_2 along with distribution of charge density differences from side view on the Kagome surface of FeSn. The blue and yellow areas represent electron depletion and electron accumulation, respectively. **b** Molecular orbitals of approximately free N_2. **c** PDOS of N_2 and the Fe-d_{z^2} orbital after N_2 adsorption. **d** PDOS of N_2 and the Fe-d_{xz}/d_{yz} orbitals after N_2 adsorption.

mechanism[51]. Our detailed Bader charge analysis further reveals a significant electron transfer of 0.52 e^- from FeSn to N_2.

To learn more insights into the adsorption mechanism of N_2 on the Kagome surface, we conduct comparative PDOS analyses. First, as a reference system, we consider an isolated N_2 molecule sufficiently far from the Kagome surface, showing the highest occupied σ orbital and lowest unoccupied π^* orbital, as shown in Fig. 2b. Upon N_2 adsorption on the Kagome surface, we observe hybridization between the Fe-d_{z^2} orbital and σ orbital of the N_2 molecule (Fig. 2c), whereas the Fe-d_{xz}/d_{yz} orbitals display significant hybridization with the occupied π orbital and unoccupied high-energy π^* orbital (Fig. 2d), with the coupling resulting from the allowed symmetry of the molecular orbitals. The back-donation mechanism is also confirmed by the partially occupied d-π^* orbital. While these analyses are consistent with chemical principles, our objective is to investigate the physical basis underlying the enhanced N_2 adsorption on the Kagome surface. To do so, we investigate the PDOS changes during the adsorption process. The comparison is made between the PDOS at the adsorption site and that at an Fe site distant from the adsorption site, as defined in Supplementary Fig. S1. From Fig. 3a, we observe significant changes in the PDOS of the d_{z^2} orbital, which predominantly contributes to the flat bands. The d_{xz}/d_{yz} orbitals also show notable changes in the PDOS near the Fermi level, whereas the in-plane $d_{xy}/d_{x^2-y^2}$ components remain virtually unchanged throughout the process, as displayed in Supplementary Figs. S2 and Fig. S3. These observations underscore the pivotal role played by the flat bands during the N_2 adsorption process on FeSn.

Subsequent steps of the ammonia production

To complete the ammonia production cycle, we further investigate the process after N_2 activation. We observe that subsequent intermediates of the eNRR do not adsorb on the on-top site of Fe but instead occupy the hollow or bridge sites of Fe, as shown in Fig. 4. We conjecture that after N_2 activation, the adsorption of subsequent intermediates depends significantly on the charge donation capability of the catalysts. In extensive prior studies, it has been consistently observed that the adsorption of the N_2H^* intermediate typically represents the rate-limiting step in the whole eNRR process[8,9]. In our present study, when adsorbed at the hollow site, the N atoms maximize their interaction with the host, thereby significantly lowering the associated energy barrier to be comparable to that in the well-studied eNRR process on a Ru (0001) surface[8]. Similar observations are evident in the charge density difference diagrams for the adsorption configurations of the subsequent intermediates, as shown in Supplementary Fig. S4.

In analogy to the analysis of N_2 adsorption discussed above, we have further monitored the changes in PDOS for the subsequent steps of the ammonia production. We find that the PDOS contributions from the d_{z^2} orbital exhibit the most significant variations in each subsequent reaction step, and notable changes in the PDOS of the d_{xz}/d_{yz} orbitals are also observed, highlighting the critical involvement of the flat bands, as shown in Fig. 3b–f and Supplementary Figs. S2 and S3. In Fig. 4, we illustrate the free energy barrier diagram for the distal pathway of eNRR. The overall limiting potential is 0.31 V, which surpasses the performance of the most efficient noble metal surfaces for eNRR activity[8]. As for the alternating mechanism, the limiting potential is higher (0.98 V), indicating that the distal mechanism dominates, and the corresponding Gibbs free energy diagram is presented in Supplementary Fig. S5. Based on these analyses, we conclude that the flat bands of the Kagome surface play a critical role throughout the entire eNRR process, as anticipated.

Robustness of the catalytic activity of Kagome-terminated FeSn

To elucidate the advantages of the natural Kagome FeSn system compared to artificially anchored single or few-atom catalysts, we explore the catalytic activity of the Kagome surface at varying adsorbate coverage. Considering the equivalence of the Fe atoms on the Kagome surface, we focus on the 2 × 2 supercell configuration. Here, each Kagome layer contains 12 Fe atoms organized into triangular units, with 4 such units per supercell, as illustrated in Fig. 5a. To investigate the impact of the adsorbate coverage and validate the independence between the neighboring active sites, we vary the number of N^* species (ranging from 0 to 3) occupying the reaction units, and assess the adsorption capacity of the remaining vacant sites for N_2. As shown in Fig. 5b–d, when pre-adsorbing 0 to 3 N^* species, the corresponding adsorption energies ΔE_{N_2} are −0.74, −0.66, −0.66, and −0.62 eV, respectively, confirming that these individual sites indeed exhibit sufficient independence in their reactivity. Overall, the atomic utilization efficiency of the monolayer reaches 25% (namely, 4 active units among the 16 atoms). Compared to the atomic percentage (at%) concept within the SACs framework, we conclude that the present system exhibits superior performance as an eNRR catalyst.

Going further into the underlying mechanism, we explore the potential impact of spin polarization on the reaction dynamics. As hypothesized,

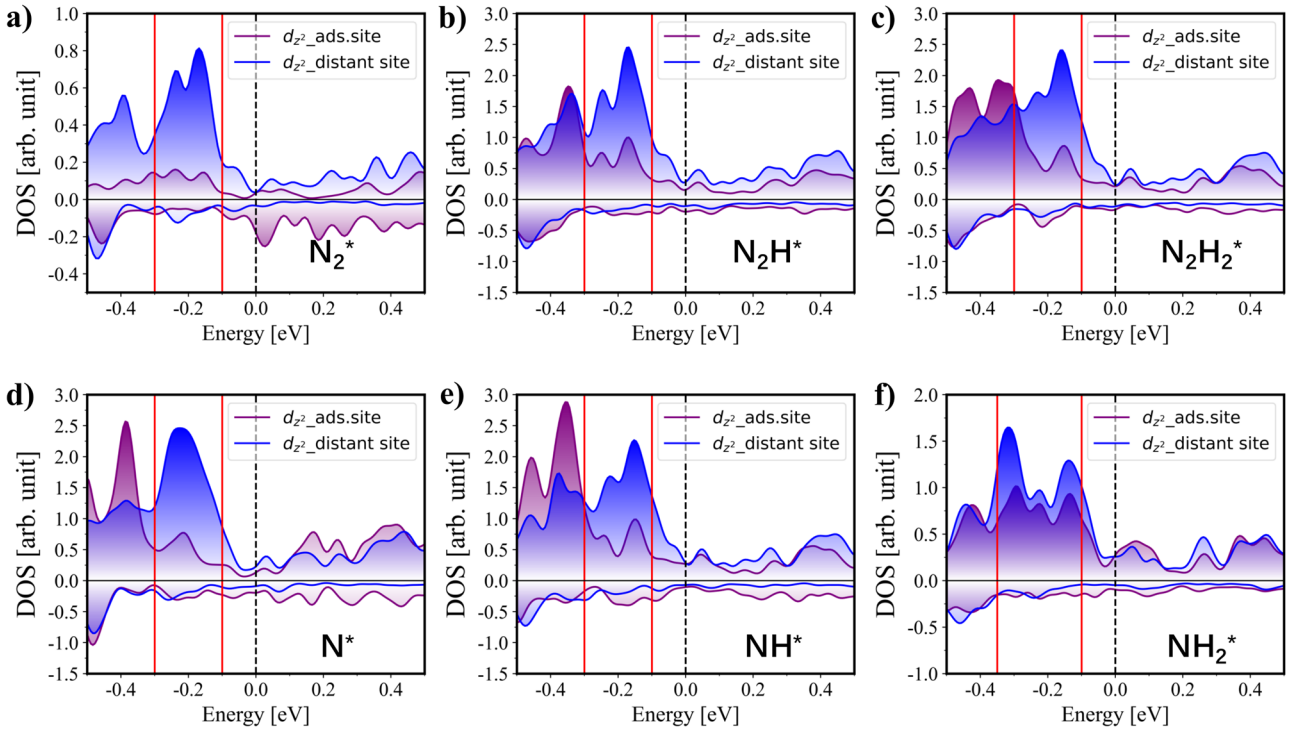

Fig. 3 | PDOS analysis for various nitrogen species adsorbed on Kagome-terminated FeSn. PDOS of the Fe-d_{z^2} orbital of the adsorption site (purple) and distant site (blue) after adsorption of **a** N_2^*, **b** N_2H^*, **c** $N_2H_2^*$, **d** N^*, **e** NH^*, and **f** NH_2^*. The definitions of different sites are presented in Supplementary Fig. S1.

Fig. 4 | Free energy diagram for the distal pathway of eNRR on Kagome-terminated FeSn. Free energy diagram as well as the optimized geometric configurations of different intermediates in the eNRR process, with an overall limiting potential of 0.31 V. In Figs. 4 and 5, the different atoms are indicated by the same color codes as in Fig. 1.

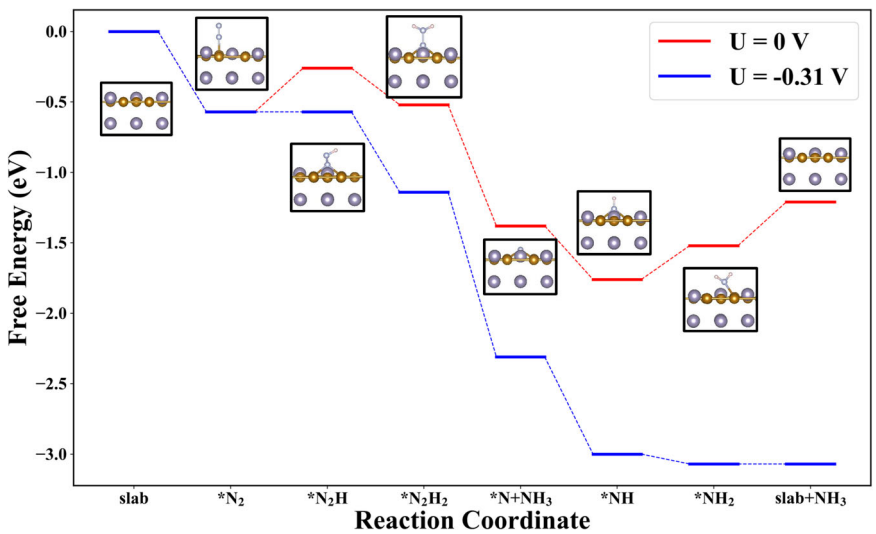

according to Hund's rule, electrons occupying the empty π^* orbital of N_2 tend to favor parallel spin alignment, suggesting that spin-polarized electrons from the catalyst may lower the reaction barriers. In our DFT calculations, the Fe atoms in the surface Kagome layer carry spin-down magnetic moments, as shown in Supplementary Fig. S6, while the flat bands depicted in Fig. 1d exhibit spin-up polarization. We also present the magnetic moment carried by each intermediate species after its adsorption in Supplementary Table S2. Although not prominently pronounced, each intermediate species shows a spin-up magnetic moment, where N_2^* carries a magnetic moment of $+0.1\ \mu_B$, and N_2H^* carries a magnetic moment of $+0.17\ \mu_B$. These results not only underscore that the flat band plays a predominant role in the interaction with the adsorbate but also further indicate the preference for spin-polarized electrons in these reaction pathways.

Here, it is worthwhile to note that solvent effects and electrode potential effects can both influence the calculated results for catalytic processes[52–54]. To investigate these effects on the catalytic activity of FeSn, we conduct additional calculations by incorporating solvent effects using an implicit solvent model and constant potential calculations using the grand canonical ensemble DFT (GCE-DFT) approach[55,56]. The corresponding free energy changes for the eNRR catalytic process are presented in Supplementary Tables S3 and S4. Although these factors slightly modify the free energy changes for the steps of the eNRR process, the main conclusions remain unchanged. Moreover, neither the solvent effects nor the electrode potential effects alter the underlying catalytic mechanisms of the Kagome surface of FeSn, particularly the critical role of the flat bands in the eNRR process. For the HER process, these effects are shown to be negligible. In addition, eNRR

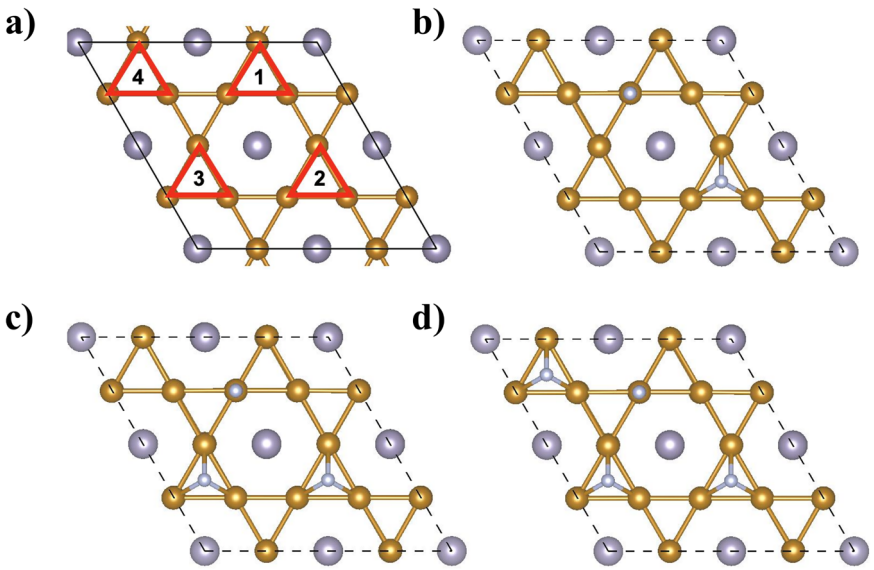

Fig. 5 | N_2 Adsorption on the Kagome surface with different N^* coverage. a Four triangular units defined in the 2 × 2 supercell of the Kagome Fe_3Sn layer. Configurations of N_2 adsorption on the Kagome surface pre-adsorbed with **b** one N^*, **c** two N^*, and **d** three N^*.

activity is influenced by both the reaction kinetics and thermodynamics. To obtain the reaction kinetics for electrocatalytic processes, explicit solvent modeling should be employed, such as by explicitly incorporating water layers[52,53], which would significantly increase the complexity and computational cost. Instead, many previous studies of electrocatalysis have suggested that the computational framework based on the computational hydrogen electrode (CHE) model, as adopted in this study, can provide reasonably accurate predictions of the reaction trends[57,58].

To assess the selectivity of eNRR over HER on FeSn, we show the Faradaic efficiency, as employed in previous literature[16]. The Faradaic efficiency of eNRR can be expressed as

$$f_{\mathrm{NRR}} = \frac{100\%}{1 + e^{\frac{-\delta G}{k_B T}}}, \tag{1}$$

where δG denotes the Gibbs free energy difference between the potential-determining steps of HER and eNRR at 0 V vs. the standard hydrogen electrode (SHE), k_B represents the Boltzmann constant, and T is taken as the room temperature and is set to be 298.15 K. For a catalytic reaction, among all elementary steps, the step with the highest ΔG defines the potential-determining step, and this ΔG value corresponds to the limiting potential (vs. SHE). For HER, the hydrogen adsorption energy is calculated to be −0.92 eV, and thereby the limiting potential is determined to be 0.74 eV; for eNRR, the limiting potential is 0.31 eV. The calculated value of f_{NRR} is essentially 100%, demonstrating the high selectivity of FeSn toward eNRR. A comparison of the volcano plots for HER and eNRR on transition metals indicates that noble-metal-based eNRR catalysts intrinsically suffer from low selectivity, as the HER pathway invariably dominates on their surfaces[5,7,8,16,18]. In contrast, the present Kagome system exhibits markedly superior performance, with the limiting potential for eNRR being significantly lower than that for HER.

Catalytic activity of other Kagome materials for eNRR

In order to substantiate the general applicability of the significant conclusion regarding the catalytic activity of Kagome flat bands in eNRR, we conduct related studies of the two isostructural Kagome materials CoSn and FeGe. We find that both CoSn and FeGe exhibit N_2 adsorption capabilities, with the adsorption energies of −0.81 and −0.50 eV, respectively. Further investigations of the overall eNRR process on their Kagome terminations show that the limiting potential barriers are 0.70 and 0.68 eV through the distal mechanism, respectively. The corresponding free energy barrier diagrams are displayed in Supplementary Figs. S9 and S11, and the optimized geometric configurations of diverse intermediates along the distal pathway are shown in Supplementary Figs. S10 and S12. As expected, due to differences in electron counting and magnetic states, CoSn and FeSn show variations in their composition of the flat bands near the Fermi level. In the energy range of −0.3 to 0 eV, the d_{xz}/d_{yz} orbitals make predominant contributions to the flat bands of CoSn, whereas the $d_{xy}/d_{x^2-y^2}$ orbitals also contribute to the flat bands near the Fermi level, as shown in Supplementary Fig. S13. Upon N_2 adsorption, we observe significant variations in the PDOS associated with the d_{xz}/d_{yz} and $d_{xy}/d_{x^2-y^2}$ orbitals, whereas the d_{z^2} orbital, which does not significantly contribute to the flat bands, shows relatively minimal PDOS changes near the Fermi level (see Supplementary Figs. S14–S16). These findings further confirm that the flat bands can consistently dominate the overall chemical process, rather than being restricted to certain specific orbitals. Our results not only underscore the significant role of flat bands but also provide constructive guidance for the targeted design of catalysts based on Kagome structures.

Discussion

In summary, we have identified that FeSn, a Kagome material, can function as a highly efficient catalyst for eNRR, with naturally abundant active sites, high stability and high selectivity. We have shown that the 2D Kagome surface is accompanied by the presence of surface flat electronic bands contributed by the Fe-d_{z^2} and d_{xz}/d_{yz} orbitals, resulting in chemisorption of N_2. The calculated limiting potential for the whole process is only 0.31 V through the distal pathway, indicating the system's superior eNRR catalytic activity. The underlying mechanism for this enhanced catalytic activity is attributed to the presence of flat bands. The mutual independence between neighboring reactive sites further ensures an exceptionally high 25% atomic utilization within the Kagome layer, with each active site possessing high selectivity of eNRR over competing HER. We have also generalized our design principle for efficient eNRR catalysts to the isostructural CoSn and FeGe Kagome systems, which further demonstrate the crucial role of the flat electronic bands. Overall, this work not only effectively enhances the functionalities of Kagome materials for important practical applications, but also integrates flat band physics with single-atom catalysis, offering new opportunities in catalyst design.

Methods

Density functional theory (DFT) calculations

We employed the Vienna Ab initio Simulation Package (VASP) within density functional theory (DFT) for first-principles calculations[59–61]. The Perdew–Burke–Ernzerhof (PBE) generalized gradient approximation (GGA) functional was adopted, incorporating spin polarization and DFT-D2 for van der Waals interactions[62,63]. 2 × 2 × 2 supercells were used for the

antiferromagnetic FeSn and FeGe, and a $2 \times 2 \times 4$ supercell for the paramagnetic CoSn. The convergence criteria were set at -0.01 eV/Å for force and 10^{-5} eV for energy. A 20-Å vacuum layer was applied to prevent interaction between different images. During optimization, the top four atomic layers were left free to relax, while the remaining four layers were fixed. Bader charge analysis was employed to investigate the charge transfer processes[64].

The adsorption energy of N_2 is defined as:

$$\Delta E_{N_2} = E_{sub+N_2} - E_{sub} - E_{N_2}, \quad (2)$$

where E_{sub+N_2}, E_{sub}, and E_{N_2} are the total energies of the combined system, substrate, and an isolated N_2, respectively. The change in Gibbs free energy, ΔG, for each elementary step was determined within the computational hydrogen electrode (CHE) framework[65], given by:

$$\Delta G = \Delta E + \Delta E_{ZPE} - T\Delta S. \quad (3)$$

Here, ΔE represents the energy difference between the product and reactants; ΔE_{ZPE} and ΔS denote the changes in zero-point energy and entropy, respectively, which are determined from vibrational frequency calculations; T is the temperature. Detailed descriptions are presented in Part I of the SI.

Solvent effects were incorporated into the DFT calculations by utilizing the VASPsol code[66,67], implemented in VASP. VASPsol employs an implicit solvent model, which describes the solvent environment through continuous dielectric properties rather than by explicitly representing individual solvent molecules. This approach minimizes the computational overhead associated with explicitly modeling solvent molecules, while still capturing the essential physics of solvent–solute interactions.

The grand canonical ensemble density functional theory (GCE-DFT) constant potential calculations[55,56] were carried out within the VASP software. The electrode potential was fixed by adjusting the total number of electrons in the system via the "NELECT" parameter in VASP. The absolute electrode potential (Φ_e) is determined by the following equation:

$$\Phi_e = \Phi_w - E_F, \quad (4)$$

where Φ_w represents the work function of the system, and E_F is the Fermi level. The absolute electrode potential relative to the SHE, denoted as U_{SHE}, is further defined as:

$$eU_{SHE} = \Phi_e - \Phi_{SHE}. \quad (5)$$

Here, Φ_{SHE} has been experimentally determined to be approximately 4.44 eV, and e is the elementary charge. Then, the grand potential Ω is defined as:

$$\Omega = E_{tot} + \Phi_e N_e, \quad (6)$$

where E_{tot} is the total energy of the system, and N_e is the total number of electrons.

Data availability

Data is provided within the manuscript or supplementary information files.

Received: 22 October 2024; Accepted: 20 May 2025;
Published online: 28 May 2025

References

1. Kitano, M. et al. Ammonia synthesis using a stable electride as an electron donor and reversible hydrogen store. *Nat. Chem.* **4**, 934–940 (2012).
2. Chen, J. G. et al. Beyond fossil fuel-driven nitrogen transformations. *Science* **360**, eaar6611 (2018).
3. Suryanto, B. H. R. et al. Challenges and prospects in the catalysis of electroreduction of nitrogen to ammonia. *Nat. Catal.* **2**, 290–296 (2019).
4. Zhao, R. et al. Recent progress in the electrochemical ammonia synthesis under ambient conditions. *EnergyChem* **1**, 100011 (2019).
5. Hoffman, B. M., Lukoyanov, D., Yang, Z.-Y., Dean, D. R. & Seefeldt, L. C. Mechanism of nitrogen fixation by nitrogenase: the next stage. *Chem. Rev.* **114**, 4041–4062 (2014).
6. Yang, X. et al. Mechanistic Insights into electrochemical nitrogen reduction reaction on vanadium nitride nanoparticles. *J. Am. Chem. Soc.* **140**, 13387–13391 (2018).
7. Foster, S. L. et al. Catalysts for nitrogen reduction to ammonia. *Nat. Catal.* **1**, 490–500 (2018).
8. Skúlason, E. et al. A theoretical evaluation of possible transition metal electrocatalysts for N_2 reduction. *Phys. Chem. Chem. Phys.* **14**, 1235–1245 (2012).
9. Montoya, J. H., Tsai, C., Vojvodic, A. & Nørskov, J. K. The challenge of electrochemical ammonia synthesis: a new perspective on the role of nitrogen scaling relations. *ChemSusChem* **8**, 2180–2186 (2015).
10. Qiao, B. et al. Single-atom catalysis of CO oxidation using Pt_1/FeO_x. *Nat. Chem.* **3**, 634–641 (2011).
11. Yang, X.-F. et al. Single-atom catalysts: a new frontier in heterogeneous catalysis. *Acc. Chem. Res.* **46**, 1740–1748 (2013).
12. Zhang, W., Fu, Q., Luo, Q., Sheng, L. & Yang, J. Understanding single-atom catalysis in view of theory. *JACS Au* **1**, 2130–2145 (2021).
13. Li, X.-F. et al. Conversion of dinitrogen to ammonia by FeN_3-embedded graphene. *J. Am. Chem. Soc.* **138**, 8706–8709 (2016).
14. Zhao, J. & Chen, Z. Single Mo atom supported on defective boron nitride monolayer as an efficient electrocatalyst for nitrogen fixation: a computational study. *J. Am. Chem. Soc.* **139**, 12480–12487 (2017).
15. Ling, C., Niu, X., Li, Q., Du, A. & Wang, J. Metal-free single atom catalyst for N_2 fixation driven by visible light. *J. Am. Chem. Soc.* **140**, 14161–14168 (2018).
16. Liu, X., Jiao, Y., Zheng, Y., Jaroniec, M. & Qiao, S.-Z. Building up a picture of the electrocatalytic nitrogen reduction activity of transition metal single-atom catalysts. *J. Am. Chem. Soc.* **141**, 9664–9672 (2019).
17. Logadottir, A. et al. The Brønsted–Evans–Polanyi relation and the volcano plot for ammonia synthesis over transition metal catalysts. *J. Catal.* **197**, 229–231 (2001).
18. Seh, Z. W. et al. Combining theory and experiment in electrocatalysis: Insights into materials design. *Science* **355**, eaad4998 (2017).
19. Liu, J.-C. et al. Heterogeneous Fe_3 single-cluster catalyst for ammonia synthesis via an associative mechanism. *Nat. Commun.* **9**, 1610 (2018).
20. Chen, Z. W., Yan, J.-M. & Jiang, Q. Single or double: Which is the altar of atomic catalysts for nitrogen reduction reaction?. *Small Methods* **3**, 1800291 (2019).
21. Lv, X., Wei, W., Huang, B., Dai, Y. & Frauenheim, T. High-throughput screening of synergistic transition metal dual-atom catalysts for efficient nitrogen fixation. *Nano Lett.* **21**, 1871–1878 (2021).
22. Cui, C., Zhang, H., Cheng, R., Huang, B. & Luo, Z. On the nature of three-atom metal cluster catalysis for N_2 reduction to ammonia. *ACS Catal.* **12**, 14964–14975 (2022).
23. Lv, X. et al. Three-dimensional dual-site catalysts for industrial ammonia synthesis at dramatically decreased temperatures and pressures. *ACS Catal.* **13**, 13561–13568 (2023).
24. Pu, T. et al. Dual atom catalysts for energy and environmental applications. *Angew. Chem. Int. Ed.* **62**, e202305964 (2023).
25. Wang, A., Li, J. & Zhang, T. Heterogeneous single-atom catalysis. *Nat. Rev. Chem.* **2**, 65–81 (2018).
26. Xiong, Y. et al. Gram-scale synthesis of high-loading single-atomic-site Fe catalysts for effective epoxidation of styrene. *Adv. Mater.* **32**, e2000896 (2020).
27. Han, L. et al. A single-atom library for guided monometallic and concentration-complex multimetallic designs. *Nat. Mater.* **21**, 681–688 (2022).
28. Syozi, I. Statistics of Kagome lattice. *Prog. Theor. Phys.* **6**, 306–308 (1951).

29. Lieb, E. H. Two theorems on the Hubbard model. *Phys. Rev. Lett.* **62**, 1927–1927 (1989).
30. Mielke, A. Ferromagnetic ground states for the Hubbard model on line graphs. *J. Phys. A Math. Gen.* **24**, L73–L77 (1991).
31. Yin, J.-X., Lian, B. & Hasan, M. Z. Topological Kagome magnets and superconductors. *Nature* **612**, 647–657 (2022).
32. Wang, Q., Lei, H., Qi, Y. & Felser, C. Topological quantum materials with Kagome lattice. *Acc. Mater. Res.* **5**, 786–796 (2024).
33. Wang, Q. et al. Large intrinsic anomalous Hall effect in half-metallic ferromagnet $Co_3Sn_2S_2$ with magnetic Weyl fermions. *Nat. Commun.* **9**, 3681 (2018).
34. Liu, E. et al. Giant anomalous Hall effect in a ferromagnetic Kagomé-lattice semimetal. *Nat. Phys.* **14**, 1125–1131 (2018).
35. Ye, L. et al. Massive Dirac fermions in a ferromagnetic Kagome metal. *Nature* **555**, 638–642 (2018).
36. Kang, M. et al. Dirac fermions and flat bands in the ideal Kagome metal FeSn. *Nat. Mater.* **19**, 163–169 (2020).
37. Lin, Z. et al. Dirac fermions in antiferromagnetic FeSn Kagome lattices with combined space inversion and time-reversal symmetry. *Phys. Rev. B.* **102**, 155103 (2020).
38. Han, M. et al. Evidence of two-dimensional flat band at the surface of antiferromagnetic Kagome metal FeSn. *Nat. Commun.* **12**, 5345 (2021).
39. Multer, D. et al. Imaging real-space flat band localization in Kagome magnet FeSn. *Commun. Mater.* **4**, 17 (2023).
40. Pham, T. A., Kang, S.-H., Ozbek, Y., Yoon, M. & Zhang, P. Distance-dependent evolution of electronic states in Kagome-honeycomb lateral heterostructures in FeSn. *ACS Nano* **18**, 8768–8776 (2024).
41. Kang, M. et al. Topological flat bands in frustrated Kagome lattice CoSn. *Nat. Commun.* **11**, 4004 (2020).
42. Liu, Z. et al. Orbital-selective Dirac fermions and extremely flat bands in frustrated Kagome lattice metal CoSn. *Nat. Commun.* **11**, 4002 (2020).
43. Huang, H. et al. Flat-band-induced anomalous anisotropic charge transport and orbital magnetism in Kagome metal CoSn. *Phys. Rev. Lett.* **128**, 096601 (2022).
44. Yin, J.-X. et al. Discovery of charge order and corresponding edge state in Kagome Magnet FeGe. *Phys. Rev. Lett.* **129**, 166401 (2022).
45. Teng, X. et al. Magnetism and charge density wave order in Kagome FeGe. *Nat. Phys.* **19**, 814–822 (2023).
46. Li, G. et al. Surface states in bulk single crystal of topological semimetal $Co_3Sn_2S_2$ toward water oxidation. *Sci. Adv.* **5**, eaaw9867 (2019).
47. Chen, H., Zhu, W., Xiao, D. & Zhang, Z. CO oxidation facilitated by robust surface states on Au-covered topological insulators. *Phys. Rev. Lett.* **107**, 056804 (2011).
48. Li, L., Zeng, J., Qin, W., Cui, P. & Zhang, Z. Tuning the hydrogen activation reactivity on topological insulator heterostructures. *Nano Energy* **58**, 40–46 (2019).
49. Huang, L. et al. Discovery and construction of surface Kagome electronic states induced by *p-d* electronic hybridization in $Co_3Sn_2S_2$. *Nat. Commun.* **14**, 5230 (2023).
50. Zhang, Y. et al. Engineering spin polarization of the surface-adsorbed Fe atom by intercalating a transition metal atom into the MoS_2 bilayer for enhanced nitrogen reduction. *JACS Au* **4**, 1509–1520 (2024).
51. Zou, H. et al. Low-valence metal single atoms on graphdiyne promotes electrochemical nitrogen reduction via M-to-N_2 Π-backdonation. *Adv. Funct. Mater.* **32**, 2200333 (2022).
52. Wu, T., Melander, M. M. & Honkala, K. Coadsorption of NRR and HER intermediates determines the performance of Ru-N_4 toward electrocatalytic N_2 reduction. *ACS Catal.* **12**, 2505–2512 (2023).
53. Wu, T., Melander, M. M. & Honkala, K. Theoretical advances in understanding the active site microenvironment toward the electrocatalytic nitrogen reduction reaction in aqueous media. *Curr. Opin. Electrochem.* **42**, 101383 (2023).
54. Tezak, C. R. et al. Revised nitrogen reduction scaling relations from potential-dependent modeling of chemical and electrochemical steps. *ACS Catal.* **13**, 12894–12903 (2023).
55. Sundararaman, R., Goddard, W. A. III & Arias, T. A. Grand canonical electronic density-functional theory: Algorithms and applications to electrochemistry. *J. Chem. Phys.* **146**, 114104 (2017).
56. Melander, M. M., Kuisma, M. J., Christensen, T. E. K. & Honkala, K. Grand-canonical approach to density functional theory of electrocatalytic systems: Thermodynamics of solid-liquid interfaces at constant ion and electrode potentials. *J. Chem. Phys.* **150**, 041706 (2019).
57. Feng, X. et al. Hydrogen radical-induced electrocatalytic N_2 reduction at a low potential. *J. Am. Chem. Soc.* **145**, 10259–10267 (2023).
58. Dai, T. Y., Wang, T. H., Wen, Z. & Jiang, Q. Recent progress on computation-guided catalyst design for highly efficient nitrogen reduction reaction. *Adv. Funct. Mater.* **34**, 2400773 (2024).
59. Hohenberg, P. & Kohn, W. Inhomogeneous electron gas. *Phys. Rev.* **136**, B864–B871 (1964).
60. Kohn, W. & Sham, L. J. Self-consistent equations including exchange and correlation effects. *Phys. Rev.* **140**, A1133–A1138 (1965).
61. Kresse, G. & Furthmüller, J. Efficient iterative schemes for ab initio total-energy calculations using a plane-wave basis set. *Phys. Rev. B* **54**, 11169–11186 (1996).
62. Perdew, J. P., Burke, K. & Ernzerhof, M. Generalized gradient approximation made simple. *Phys. Rev. Lett.* **77**, 3865–3868 (1996).
63. Grimme, S. GGA-type density functional constructed with a long-range dispersion correction. *J. Comput. Chem.* **27**, 1787–1799 (2006).
64. Tang, W., Sanville, E. & Henkelman, G. A grid-based Bader analysis algorithm without lattice bias. *J. Phys.***21**, 084204 (2009).
65. Nørskov, J. K. et al. Origin of the overpotential for oxygen reduction at a fuel-cell cathode. *J. Phys. Chem. B* **108**, 17886–17892 (2004).
66. Mathew, K., Sundararaman, R., Letchworth-Weaver, K., Arias, T. A. & Hennig, R. G. Implicit solvation model for density-functional study of nanocrystal surfaces and reaction pathways. *J. Chem. Phys.* **140**, 084106 (2014).
67. Mathew, K., Kolluru, V. S., Mula, S., Steinmann, S. N. & Hennig, R. G. Implicit self-consistent electrolyte model in plane-wave density-functional theory. *J. Chem. Phys.* **151**, 234101 (2019).

Acknowledgements

This work was supported by National Natural Science Foundation of China (Grants Nos. 12374458, 12488101, and 11974323), the Innovation Program for Quantum Science and Technology (Grant No. 2021ZD0302800), and the Strategic Priority Research Program of Chinese Academy of Sciences (Grant No. XDB0510200).

Author contributions

P.C. and Z.Z. co-supervised the project. Y. H. performed the calculations with helps from Y. C. and S. Z. All authors analyzed the data, discussed the results, and improved on the paper.

Competing interests

The authors declare no competing interests.

Additional information

Supplementary information The online version contains supplementary material available at https://doi.org/10.1038/s41524-025-01663-w.

Correspondence and requests for materials should be addressed to Zhenyu Zhang or Ping Cui.

Reprints and permissions information is available at http://www.nature.com/reprints

Publisher's note Springer Nature remains neutral with regard to jurisdictional claims in published maps and institutional affiliations.

Open Access This article is licensed under a Creative Commons Attribution-NonCommercial-NoDerivatives 4.0 International License, which permits any non-commercial use, sharing, distribution and reproduction in any medium or format, as long as you give appropriate credit to the original author(s) and the source, provide a link to the Creative Commons licence, and indicate if you modified the licensed material. You do not have permission under this licence to share adapted material derived from this article or parts of it. The images or other third party material in this article are included in the article's Creative Commons licence, unless indicated otherwise in a credit line to the material. If material is not included in the article's Creative Commons licence and your intended use is not permitted by statutory regulation or exceeds the permitted use, you will need to obtain permission directly from the copyright holder. To view a copy of this licence, visit http://creativecommons.org/licenses/by-nc-nd/4.0/.

© The Author(s) 2025